STRUCTURAL CONTROL AND HEALTH MONITORING
Struct. Control Health Monit. 2016; **23**:802–824
Published online 2 November 2015 in Wiley Online Library (wileyonlinelibrary.com). DOI: 10.1002/stc.1811

Proof of concept of the structural health monitoring of framed structures by a novel combined experimental and theoretical approach

D. Isidori[1,2], E. Concettoni[2], C. Cristalli[2], L. Soria[3] and S. Lenci[1,*,†]

[1]*Università Politecnica delle Marche, Dipartimento di Ingegneria Civile Edile e Architettura, Via Brecce Bianche 60131 Ancona, Italy*
[2]*Loccioni Group, R&I Department, Via Fiume 16, 60030, Angeli di Rosora, Ancona, Italy*
[3]*Dipartimento di Meccanica, Matematica e Management, Politecnico di Bari, Viale Japigia 182, 70126 Bari, Italy*

SUMMARY

One of the most important issues in engineering is the detection of structural damages. During its life cycle, a building, besides the exposure to operational and environmental forces, can be subjected to earthquakes or to other non-ordinary loads. These events may have a deep impact on the building safety, and thus, a continuous monitoring of the structure health conditions becomes desirable or even necessary in many cases. In this context, the usage of vibration-based structural health monitoring (SHM) systems is spreading from big infrastructures applications, like bridges, dams or skyscrapers, to the historical heritage and to public or residential buildings. The aim of this work is to propose a combined experimental and numerical methodology to perform the SHM of structures of the civil engineering lying in seismic hazard zones. A relatively low cost SHM prototype system based on this approach is developed. The data acquired by the system are provided to a finite element method (FEM) numerical model to detect the appearing, the rise and the distribution of local damages and to estimate a global damage level. The system has been tested and calibrated on a three-storey prototype model. The procedure for the estimation of the damage level is calibrated by comparing the experimental quantities measured during cyclic failure tests with the FEM model predictions. Copyright © 2015 John Wiley & Sons, Ltd.

Received 6 January 2014; Revised 2 June 2015; Accepted 25 September 2015

KEY WORDS: earthquake engineering; damage detection; structural identification; structural health monitoring; MEMS sensors

1. INTRODUCTION

One of the most important goals of structural engineering is to provide an adequate level of safety against damage occurring during earthquakes [1]. For this reason, monitoring the health condition of a structure is crucial for building safety [2]. Nowadays, theoretical and experimental research efforts entailing the seismic behaviour of structures are available [3], as different attempts leading to the quantitative estimation of damage degree [4,5], obtained by using the so-called damage indices. The most important issue in this approach is related to the calibration of each index, by using experimental data [6,7].

Damage is defined as a set of modifications in either the material or the geometric features of a structure, which affect the current performance. Studies on causes of damage regard, on one side, the analysis of material behaviour, in terms of ageing or degradation, and on the other side, the structural analysis and, thus, maximum stress, maximum strain attained, and others. A well-known classification

*Correspondence to: Stefano Lenci, Università Politecnica delle Marche, Dipartimento di Ingegneria Civile Edile e Architettura, Via Brecce Bianche, 60131 Ancona, Italy.
†E-mail: lenci@univpm.it

for damage identification methods, introduced by Rytter (1993) [8], defines in particular four levels of damage identification: (i) existence, (ii) location, (iii) extent, and (iv) prediction. Consequently, a structural health monitoring (SHM) methodology aims at identifying the presence of damage and at measuring damage evolution. SHM systems provide a valuable knowledge of the dynamic behaviour of monitored structures, of their response to service and environmental loadings and of rise and distribution of deterioration conditions. These systems, widely employed in mechanical, aeronautical and civil engineering (see, e.g., [9–11]), generally rely on vibration response measurements as primary data and on several post-processing techniques [12,13]. Specifically, in vibration-based SHM, existence of damage can be detected by comparing the so-called modal parameters, that is, the natural frequencies, damping ratios and mode shapes of the damaged structure, with the corresponding parameters of the healthy structure. In fact, values of these parameters, which vibration dynamics depends upon, undergo modifications owing to damage. Basically, modal parameters are functions of the physical properties of a structure, the mass, damping and stiffness distribution, and consequently, changes in these physical properties modify the modal parameters. Several references that address damage detection and related issues have been published [14–20]. Mottershead and Friswell (1993) [21] present a survey of the literature related to finite element model (FEM) updating, which has been extensively used for structural damage detection.

The development of low-cost and low-energy measuring devices, which represent the new generation of acquisition systems, and the increasing availability of hardware and software for advanced computational analysis, have by now made possible the usage of SHM techniques, originally developed for large civil structures, as bridges, dams and skyscrapers [22], in the field of more common and diffused structures as historical, public or residential buildings. Within this background, the aim of this research is to propose a novel combined experimental and numerical methodology to perform SHM of civil and building engineering structures lying in seismic hazard zones. Specifically, we combine experimental results from vibration response measurements (used to identify the dynamic characteristic of the structure and for tuning the numerical model) with finite element analysis, in order to compute the stress–strain results through a non-linear dynamic computation. In this way, we obtain the behaviour of the structure not only by comparing the states before and after a specific important event but also by studying what happens during the event through structural analysis. Following the Rytter's classification, through this approach, we not only locate the damage and calculate the damage extent, but we also achieve the prediction of remaining service life.

In this paper, we present the preliminary results obtained by applying the proposed methodology to an in-house fabricated experimental model. In particular, with the sole aim of proving the concept, the capabilities of our approach have been tested by performing experiments, in laboratory conditions, on a three-storey aluminium scaled frame. Thus, a low-cost SHM prototypic system, based on this approach, has been developed. The proposed methodology comprises two different phases: (i) a long-term data acquisition, aimed at revealing slow modifications of structural features that through updating of numerical model parameters allows for detecting damage because of ageing and (ii) an instantaneous survey, aimed at estimating the health of a structure next to some particular events as strong overloads, occurring during earthquakes. We are aware that in the present experimental work we are overlooking the environmental effects that could affect the dynamic response [11]. However, because the scope of the paper is to check the method, this important issue is left for future work. The approach requires a preliminary set-up of both the diagnostic system and the theoretical model (Figure 1). The former specifically includes the data acquisition system set-up and calibration of accelerometers.

The theoretical model set-up requires tuning of the FEM, through a preliminary identification of modal parameters, the study of hysteretic properties of materials and a survey of damage characteristics. The formalisation of a theory, which describes the mechanical behaviour of materials and structures because of cyclic loading in the elastic–plastic range, must embrace two complementary aspects: (i) the correct definition of appropriate criteria for collapse and (ii) the introduction of effective models of cyclic behaviour, which are able to realistically simulate the non-linear local and global evolutionary response [23].

Because a global or a local kind of collapse can generally take place in a structure, typically two types of damage index have to be adopted for detection [24,25]. The evolution of an initial local failure from element to element may cause progressive global collapse [26]. Global collapse may involve

DOI: 10.1002/stc

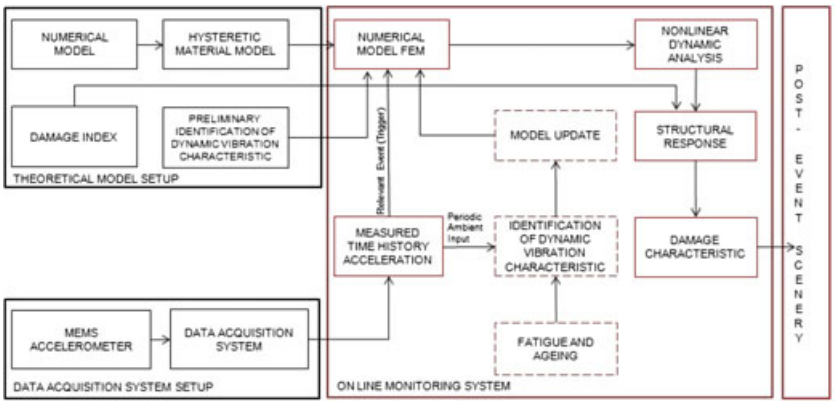

Figure 1. Flow chart of the SHM system.

dynamic instability, which is usually triggered by large inter-storey drifts and which is amplified by second-order effects, the so-called P-Δ effects, and by strength and stiffness deterioration of the structure [27]. Cyclic loading tests in the elastic–plastic range are, thus, requested to detect local and global damage mechanisms, studying the dynamic response of the structure, and the reliability of the numerical model when compared with experimental results. In the case of the considered structure, the local damage is commonly caused by low-cycle fatigue, while collapse is attained by the progressive accumulation of lateral drifts related to the application of a series of large inelastic deformation cycles and significant P-Δ effect [28,29].

The paper is composed of the following sections. In Section 2, we describe the experimental set-up. The considered model is a one-span three-storey aluminium frame with a soft storey behaviour at the ground floor. Although the P-Δ effects due to gravity loads are usually significant only for very high frames, the secondary effects are stressed and amplified for this particular application, as a consequence of the fact that the pillars are slender because in the experimental model we wish to have natural frequencies close to the natural frequencies of real structures. Actually, the P-Δ effects play an important role in the subsequent analysis (model updating and evaluation of the structural vulnerability). In Section 3, we report on the experimental identification of the structure, performed by operational modal analysis (OMA). In Section 4, the used numerical model is described with comparison of its results with those from operational modal analysis (OMA). In Section 5, we introduce the adopted local and global damage indexes, while, in Section 6, we discuss results from the proposed SHM approach. Concluding remarks are summarised in Section 7. Analytical results obtained in the case of a clamped–clamped beam when considering P-Δ effect, requested for computing the adopted global damage index are reported in Appendix A.

2. THE EXPERIMENTAL SET-UP

The model is a one-span aluminium frame with three storeys and different heights (252 mm for the first storey and 172 mm for the second and third storeys). In order to increase the vulnerability of the structure at the first floor, several tests increasing the storey stiffness by rotating one, two or all the pillars of the upper floors are made. In this work, the results obtained rotating just one column in the second and in the third levels are shown, because we have not found major differences with the other cases. In this way, a typical soft storey behaviour (at the first level) is obtained, which is just what we want to obtain as this situation frequently occurs in the applications. The distances between the centroid of the pillars are 246.5 mm along x-direction and 107 mm along y-direction. The columns have a rectangular cross section (2×15 mm) and are made of a standard aluminium alloy AlMgSi 6060 with a T6 heat treatment. The frame was placed on a slip table with displacement allowed only along the x-direction. The added masses, applied on each floor (taking into account the weight of the sensors/cables) and considered in the dynamical behaviour of the frame, are equal to 0.7 kg for each pillar of the first and second floors and 0.35 kg for each pillar of the third floor. The model is shown in Figure 2.

DOI: 10.1002/stc

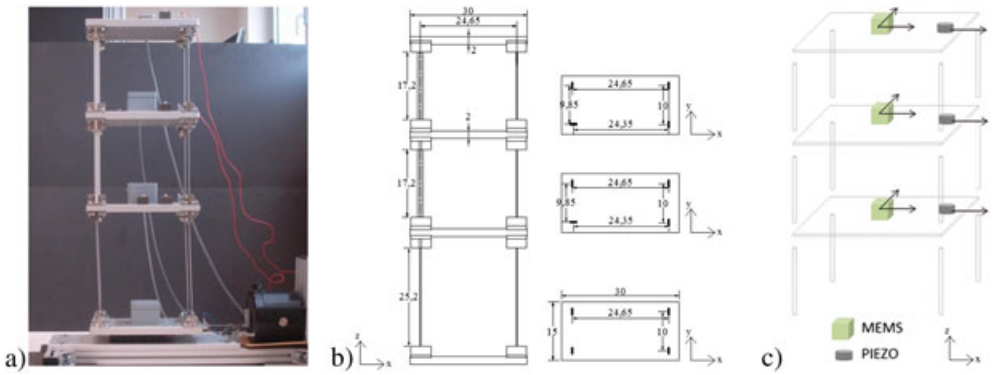

Figure 2. (a) Experimental model, (b) schematic drawing, and (c) layout of sensors and measuring direction.

The data acquisition instrumentation and interconnections between the equipment are illustrated in Figure 3. In particular, we used the following:

- An electrodynamic shaker Brüel & Kjær (B&K), Type 4809;
- A piezoelectric load cell PCB 208C01 placed between the model base and the shaker stinger to measure force at the driving point;
- Four piezoelectric Integrated Electronics Piezo Electric (IEPE) 100 mV/g accelerometers fastened to each storey. Starting from ground to top: ACC. #0 PCB 353, ACC. #1 B&K 4514–001, ACC. #2 Endevco A56-100, ACC. #3 PCB 353; and
- Two types of sensors based on micro-electro-mechanical systems (MEMS) accelerometers: A breakout board made with a Freescale Semiconductor MMA7361L 1.5 g three-axis (placed on third storey) [30] and an ST Microelectronics LIS2L02AS4 2 g two-axis linear accelerometer (the chip has been integrated in a custom electronic circuit for power supply regulation, output voltage filtering and impedance adaptation made by AEA srl – Loccioni Group) [31]. Each one has been calibrated before the experiment on a B&K 4294 exciter.

When monitoring large structures where several accelerometers are utilised, the cost of each sensor also becomes a determining element in their choice. Seismic accelerometers based on piezoelectric and piezoresistive technology are largely employed in monitoring of structures of civil engineering, but in recent years, the possibility of using capacitive MEMS accelerometers as an alternative to expensive conventional accelerometers is the subject of several studies [32,33].

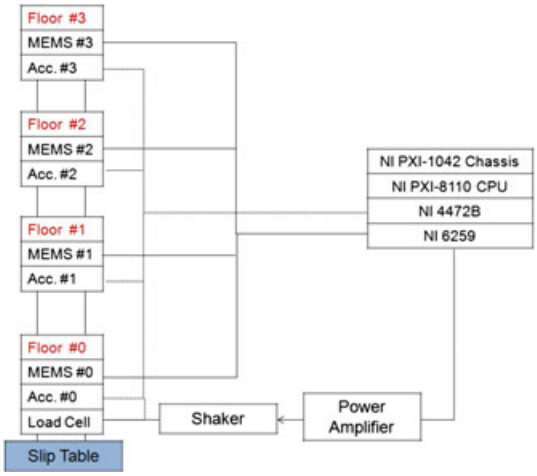

Figure 3. Experimental set-up and interconnections between the used equipment.

DOI: 10.1002/stc

For these reasons, preliminary tests have been carried out to characterise low-cost MEMS sensors. The results showed that accelerometers based on ST Microelectronics LIS2L02AS4 chip have the best performance-to-cost ratio, the highest sensitivity and the lowest floor noise [34–36].

Data were acquired with a National Instruments PXI 1042 chassis, equipped with a PXI 8110 CPU, a PXI 4472B data acquisition board (102.4 kS/s, 8 Channel, 24-Bit) for IEPE accelerometers and load cell, and a PXI 6259 (16 Analog Inputs at 16 Bits, 1.25 MS/s) for MEMS analog out acquisition and signal generation. Software for signal generation, data acquisition and analysis were developed by using National Instruments LabVIEW 2010.

3. EXPERIMENTAL IDENTIFICATION OF THE STRUCTURE

In the field of vibration-based structural identification, OMA, also referred to as output-only modal analysis, is the most suitable technique for SHM applications [9–12]. OMA, in fact, allows for the experimental identification of structures in operating conditions [37,38], leading to the evaluation of the natural frequencies, the damping factors and the mode shapes [39], without the knowledge of the excitation, but under the basic assumption that the unknown external excitation can be approximated by a combination of uncorrelated white noise sequences. In the case of large civil structures [40] or in several mechanical engineering applications [41], the environmental unknown excitation usually satisfies this assumption.

Cross power spectra (CPS) of all the measured output signals are estimated, with respect to one or more output signals selected as references, and post-processed, by using dedicated curve fitting algorithms, to obtain the modal parameters.

The identification of the dynamic behaviour of the structure plays a fundamental role in the proposed approach, because modal parameters are used to update the numerical model. Here, we report on the structural identification of the prototype model (Figure 2), performed by using an OMA approach, which is practically the sole that can be used in the case of a real multistorey building. In fact, when the specific purpose of the identification is the continuous monitoring of a structure's health, the route of input–output modal analysis, although possible, should be not followed, because OMA allows for using a simpler and less expensive set-up, not needing any specific source of external excitation (as a shaker or a vibrodyne). We, actually, hypothesise that the structures can be suitably identified by means of OMA and that, therefore, the available environmental excitation levels are high enough for making possible the output-only modal identification of the structure.

A white noise shaker input excitation has been used to load the slip table in the frequency range from 0 to 100 Hz. The time records were acquired at a sampling rate of 1000 Hz, by using a 2500-Hz low-pass anti-aliasing filter. The requisite CPS have been obtained by using the correlogram approach, by firstly estimating the correlation or covariance matrix between the measured output signals. Afterwards, the so-called weighted correlogram has been used as non-parametric spectrum estimate, computed as the discrete Fourier transform of the weighted estimated correlation matrix. With regard to the utilised frequency resolution, a value equal to 0.2 Hz has been considered suitable. Although, in fact, frequency resolutions of even one order of magnitude smaller are commonly employed in the case of high modal density real-world structures, having closely spaced modes in the dynamic response, this is not the case of the experimental model here used for proving the concept of the proposed methodology.

Among the available curve-fitting techniques, formulated in both the time domain and the frequency domain [42], the operational polyreference least square complex frequency domain modal identification technique, known as the PolyMAX algorithm [43,44], available in the LMS Test.Lab software suite (www.lmsintl.com), has been used for CPS post-processing and modal parameter estimation. In the last decade, in fact, this technique has become a valid and powerful alternative to the family of subspace methods [42,45], commonly utilised in all the applications of structural identification, and, specifically, in vibration-based SHM. In the frequency range from 0 to 35 Hz, the results obtained in terms of eigenfrequencies and damping ratios are shown in the second and the third columns of the forthcoming Table II, while the identified mode shapes are illustrated in the forthcoming Figure 11, where the corresponding modes obtained by finite element analysis are represented.

DOI: 10.1002/stc

In Figures 4–6, we report the obtained CPS, by highlighting with vertical lines the identified eigenfrequencies. Specifically, the adopted reference signals were the *x*-components of the three MEMS sensors located respectively on the first, the second and the third storey of the structure. This choice comes from the fact that the provided shaker excitation was directed along the *x*-axis. In Figure 7, the operational PolyMAX stabilisation diagram is represented [42].

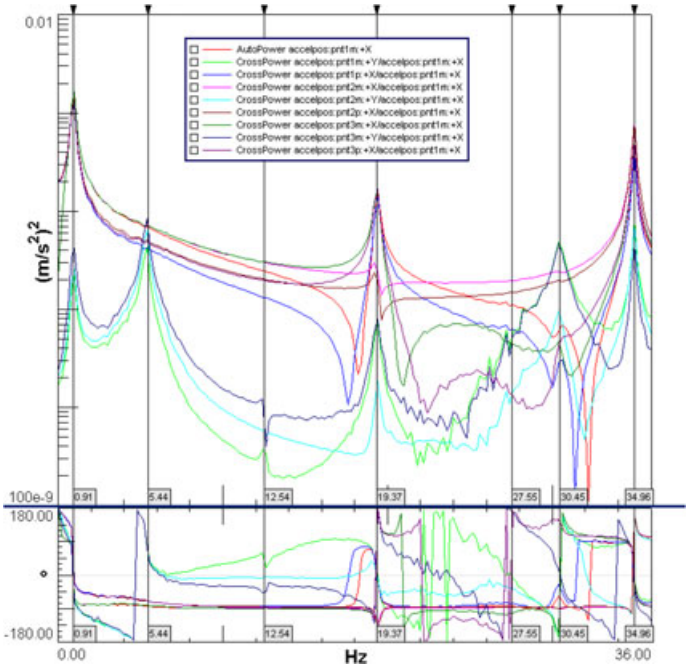

Figure 4. Cross power spectra computed with respect to the *x*-component of the first storey MEMS accelerometer. The identified eigenfrequencies are highlighted by vertical lines.

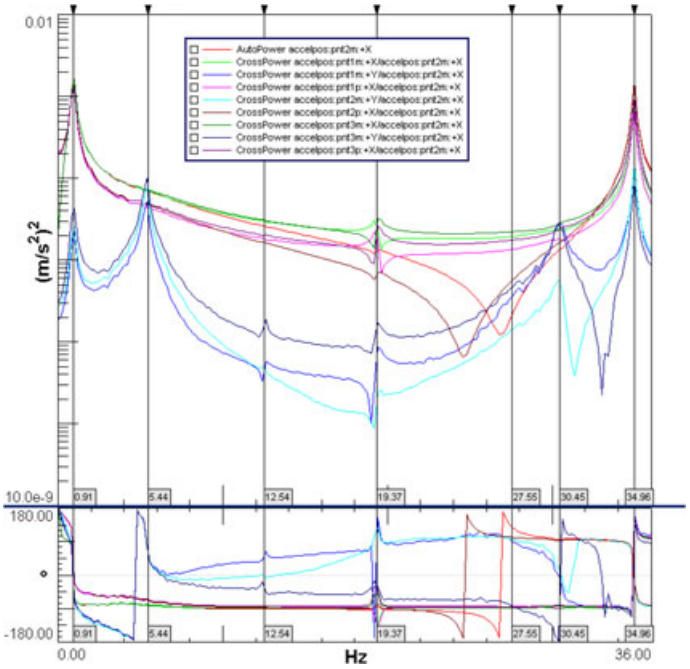

Figure 5. Cross power spectra computed with respect to the *x*-component of the second storey MEMS accelerometer. The identified eigenfrequencies are highlighted by vertical lines.

DOI: 10.1002/stc

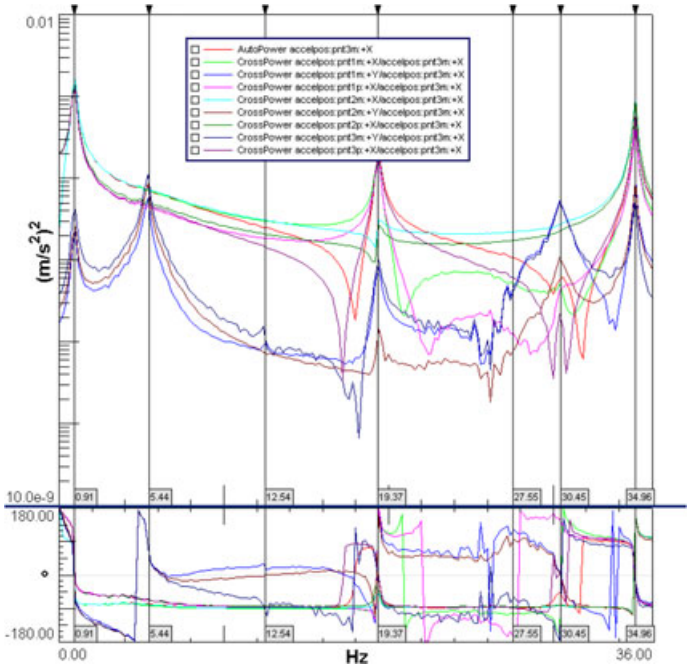

Figure 6. Cross power spectra computed with respect to the *x*-component of the third storey MEMS accelerometer. The identified eigenfrequencies are highlighted by vertical lines.

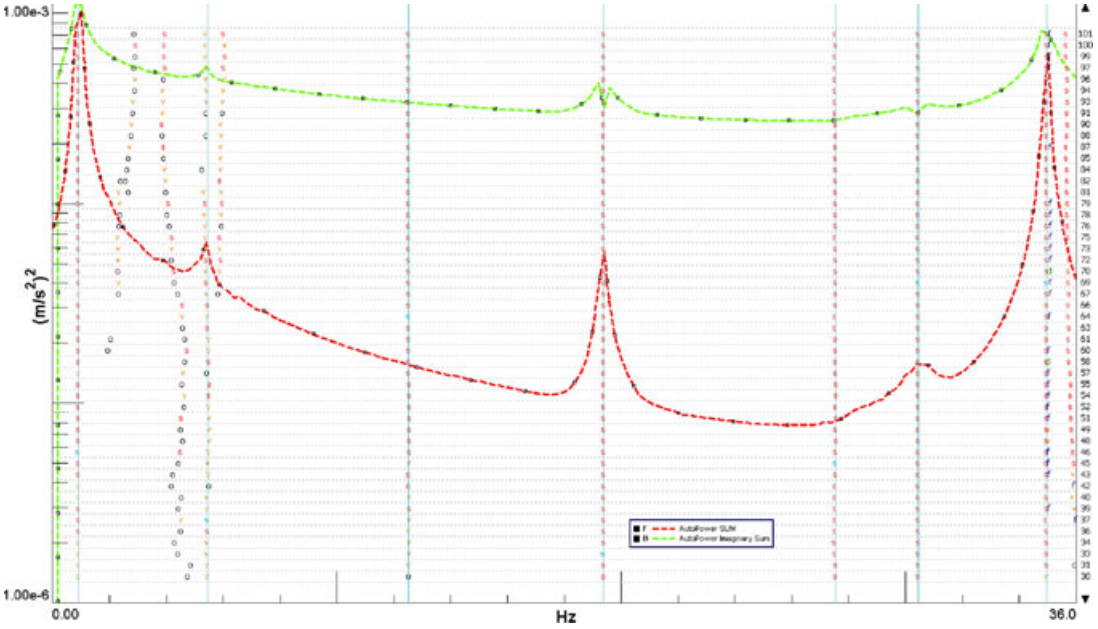

Figure 7. Operational PolyMAX stabilisation diagram. The identified stable poles are highlighted in cyan.

The diagram is very clear both because generally frequency domain techniques provide a better stabilisation and even because of the particular analysed structure behaviour. The stabilisation order rank is, in fact, quite low in all the cases.

Finally, the CPS operational syntheses have been evaluated and satisfactorily compared with the estimated ones, to validate the modal model. The correlation of synthesised and estimated CPS has been found higher than 99% for all sensors' *x*-components and higher than 90% in the case of *y*-components, a direction that is not so important for the present work. For this reason, in the following (see next Table II), we will use only the in-plane frequencies and we will not consider the out-of-plane

DOI: 10.1002/stc

modes. This choice is also supported by the fact that the out-of-plane frequencies have less accentuated peaks in Figure 7.

4. NUMERICAL MODEL

The development of increasingly sophisticated software for advanced computational analysis made it possible the use of dynamic analysis for the study of non-linear behaviour of structures during catastrophic events (as earthquakes). Non-linear dynamic analysis allows understanding what happens during a hypothetical earthquake taking into account all the dynamic features during the step-by-step integration.

The experimental model has three storeys with the typical *shear type* behaviour of the pillars. Accordingly, the same assumption is made for the numerical (FEM) model.

4.1. Material model

The mechanical properties of the alloy are obtained from the material data sheets, from nominal values [46] and from tensile tests specifically made to characterise the mechanical behaviour. They are listed in Table I. The data are used to calibrate numerical parameters in order to obtain stress–strain relationship in accordance with *Annex E* of [46].

The hysteretic material behaviour is described by the *Chaboche* model [47], which includes the isotropic and the kinematic behaviours. In the isotropic model, the yield surface undergoes a uniform expansion in the space of the principal stresses, while in the kinematic model, this surface rigidly translates during plastic deformation. Some *ad hoc* cyclic tensile–compression tests on cylindrical specimens are performed to obtain the parameters of the Chaboche hysteretic model for the considered material [48]. The associated stress–strain curves for the alloy are plotted in Figure 8.

4.2. Plasticity model

The material non-linearity is taken into account by lumped and distributed models [49,50].

Distributed plasticity model provides the more general framework for non-linear frame analysis, because non-linearities can develop anywhere along the structural element. A fibre model approach is used to simulate distributed non-linear behaviour. The representative components necessary to characterise the model are as follows: non-linear force-based FEM elements [49] for the pillars with seven sections of integration and 200 fibres to represent the cross section behaviour, rigid diaphragm constraint that approximates storey

Table I. Aluminium alloy 6060-T6 mechanical properties.

σ_y [MPa]	ε_u	E [GPa]	E_2 [GPa]	ϱ [kg/m^3]
175	0.12	66	4.3	2650

Yield strength σ_y, ultimate elongation ε_u, Young's modulus E, post yield modulus E_2, density ϱ.

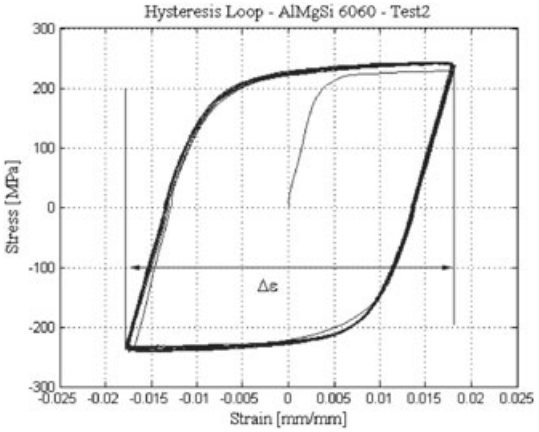

Figure 8. Cyclic stress–strain relationship [48].

DOI: 10.1002/stc

behaviour, rigid link constraint that approximates the effect of the constraint at the end of each pillar and lumped mass elements for overload (that in this case is the total overload shown in Section 2 divided for each constraint). All degrees of freedom at the bottom of the base pillars are restrained.

The lumped plasticity approach, on the other hand, is characterised by discrete plastic hinges inserted at the ends of pillars. The position of the non-linear moment–rotation hinges (non-linear link elements) and the appropriate moment–rotation relationship should be determined previously and require a lot of care. The non-linear link is active only when the moment of the corresponding cross section reaches the yield moment value. Then, the plastic behaviour is considered only on the non-linear link. In Figure 9, the calibration scheme of the non-linear link is represented.

In this case, the non-linear link is located near the restraint of a cantilever model that represents the half length of a clamped–clamped beam. The specific position of non-linear link is equal to half of equivalent plastic hinge length (Lp) calculated to determine the moment–rotation relationship. The characteristics of these plastic hinges (which are non-linear link elements and are characterised by an appropriate moment–rotation relationship) are verified by comparing the capacity curves (see the forthcoming Figure 12) of lumped and distributed plasticity models of the clamped–clamped beam (shear versus the upper floor x-displacement relationship of the two models subjected to a pushover analysis). Analytical results are reported in Appendix A.

The moment–rotation relationship of each non-linear link is represented in Figure 10. The rotation is obtained by multiplying the curvature for the plastic hinge length that in this case is considered equal to the height of the section. The material considered is the standard aluminium alloy 6060 previously described, the cross section area is equal to $A = 22.5$ mm, and the length of the cantilever is equal to $L = 126$ mm.

4.3. P-Δ effect

In flexible structures if gravity loads are large with respect to the lateral stiffness, the secondary effects become important and can change the mechanical and dynamical characteristics of the frame. Therefore,

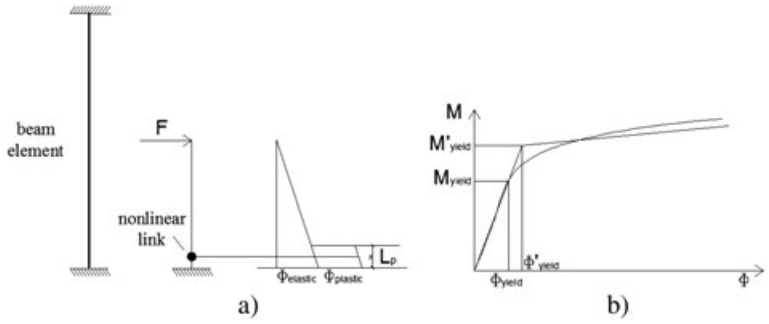

Figure 9. (a) Non-linear link calibration and (b) non-linear link static scheme.

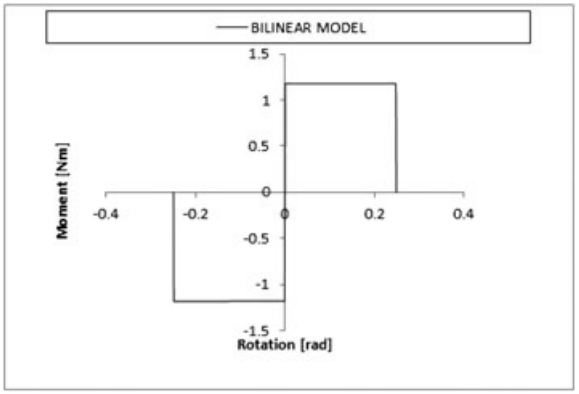

Figure 10. Moment–rotation relationship of non-linear link.

DOI: 10.1002/stc

the P-Δ effect has to be considered in the theoretical model to obtain the effective tangent stiffness and the related frequencies, in order to have a better comparison with the experimental results. The P-Δ effect can be generally determined by using a second-order analysis, and an iterative analysis is the common approach [51]. Another method for P-Δ analysis, specifically formulated for building-type structures, is the geometric stiffness method. By modifying the stiffnesses, the final analytical results match those of the iterative approach. Actually, the P-Δ effect can be linearised using this second approach because the total axial force at each storey is equal to the weight of the building above that level and does not change during the application of lateral loads [52].

Table II compares the numerical and the experimental natural frequencies. Only the first one is clearly affected by the P-Δ effect. Because of the high stiffness of the second and third storeys, the first mode shape (Figure 11) is basically a rigid body motion of the storeys over the low-level pillars; thus, all the masses are subjected to the same displacement. This does not occur for higher modes.

In Figure 11, the mode shapes are shown. The first, the fourth and the seventh frequencies correspond to the flexural modes mainly belonging to the direction of action of the shaker. The second and the sixth natural frequencies detected in the numerical model are related to the first and the second flexural modes in the direction orthogonal to the shaker, while the third and the fifth correspond to torsional modes. Notice how, in this case, only the resonance frequencies of the modal modes associated with the *x*-direction of action of the shaker are compared with the experimental results, because the aim of this research is to study the behaviour of the structure along the voluntarily made more vulnerable direction (the *x*-direction), in order to simulate real cases where frequently one has a weaker direction. For this reason, the layout of the monitoring system is designed to focus on mode shapes relative to the (*x*, *z*) plane, by neglecting, at this stage, the out-of-plane modes generated by the non-symmetrical configuration of the pillars of the upper floors (that are turned just to accentuate the difference in the floor stiffness), which are reported only to provide a general understanding of the dynamical behaviour of the structure. The identification of the out-of-plan modes will be considered in future work.

Table II. Operational modal analysis (OMA) natural frequencies $f_{n,i}^{\mathrm{OMA}}$ and damping ratios ζ_i^{OMA}, numerical natural frequencies obtained without accounting for P-Δ effect $f_{n,i}^{\mathrm{N}}$ and by taking into account P-Δ effect $f_{n,i}^{N,P-\Delta}$.

Mode	$f_{n,i}^{\mathrm{OMA}}$ [Hz]	ζ_i^{OMA} [%]	$f_{n,i}^{\mathrm{N}}$ [Hz]	$f_{n,i}^{N,P-\Delta}$ [Hz]	Maximum errors in %	Description
1	0.913	1.69	1.36	0.911	0.20	1st *x*-mode
2	—	—	7.95	7.93	—	1st torsional mode
3	—	—	10.6	10.57	—	1st *y*-mode
4	19.37	0.487	19.47	19.38	0.05	2nd *x*-mode
5	—	—	25.78	25.77	—	2nd torsional mode
6	—	—	33.79	33.72	—	2nd *y*-mode
7	34.96	0.125	35.41	35.3	0.97	3rd *x*-mode

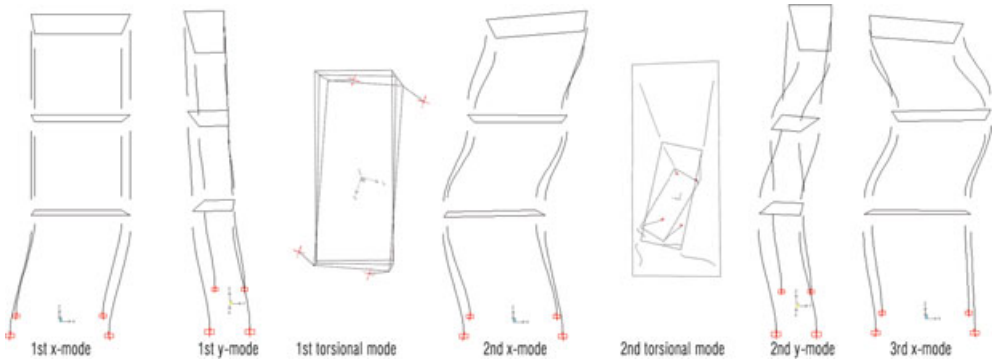

Figure 11. The first seven mode shapes obtained by using the numerical model.

DOI: 10.1002/stc

The P-Δ effects are considered also in the static behaviour of the structure, because in inelastic flexible structures, gravity loads acting together with lateral forces amplify the lateral displacements and the stresses, and thus may contribute to trigger the collapse.

The evaluation of the structural vulnerability with respect to the P-Δ effects can be obtained by a pushover analysis. During this non-linear static analysis, the structure is subjected to a lateral load distribution proportional to the first mode.

The capacity curves, representing, the base shear versus the upper storey x-displacement, are depicted in Figure 12, both with and without the P-Δ effect and with lumped and distributed plasticity models. The numerical model results are also compared with analytical clamped–clamped beam model results obtained in Appendix A.

The P-Δ effect on the pushover curve shows the following: (i) the initial reduction of the elastic stiffness (as previously discussed) and (ii) a somehow expected softening behaviour, that is, a negative stiffness in the plastic range of deformation [53].

The considered structure becomes vulnerable to collapse induced by the global P-Δ effect on the ground storey when it reaches a state with zero static lateral resistance. This happens when the displacement of the upper storeys (that is the same of the first storey in the considered prototype model) is $\Delta_{\text{lim}} = 0.092$ m (Figure 12).

5. DAMAGE INDEXES

In the presence of cyclic loads, to prevent the collapse due to plasticity is not sufficient. The structure is likely to be affected by damage accumulation, which could jeopardise the structural serviceability by leading to a decreased structural safety.

After the preliminary characterisation of the material properties and a manual tuning of the numerical model, structural responses are analysed in order to obtain damage quantification. The considered procedure is illustrated in Figure 13. Cycling loading tests are performed on the model to induce a progressive reduction of the fatigue resistance and the flexural buckling collapse of the structure (this latter being highly enhanced by the P-Δ effect).

During the test, if the stresses remain below the linear elastic limit, the only phenomenon that could lead to damage is the fatigue. On the other hand, if the plasticity thresholds are exceeded, two phenomena could cause damage: low cyclic fatigue and ratcheting behaviour, which causes plastic strain accumulation [54].

In cyclic plastic deformation, local strain oscillates between minima and maxima without changing after the first few cycles. Ratcheting plasticity, instead, produces a progressive increment of the plastic local strain at each cycle without any recovery.

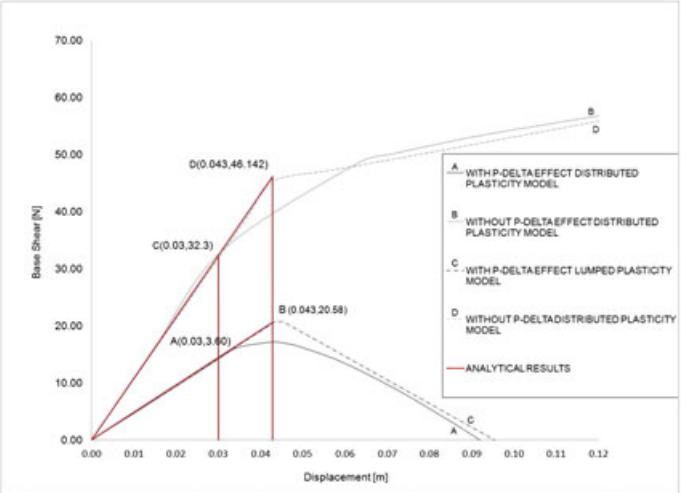

Figure 12. Comparison of capacity curves with and without the P-Δ effect, in the cases of lumped and plasticity models.

DOI: 10.1002/stc

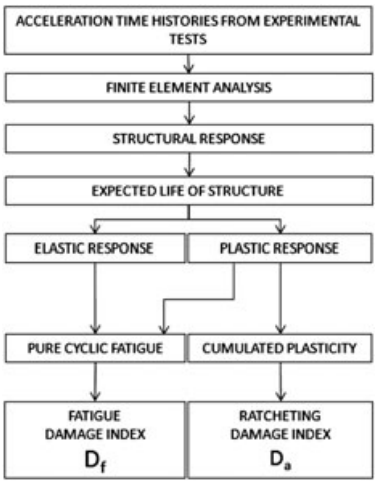

Figure 13. Flow chart of damage detection.

Therefore, the structural damage can be related to two different mechanisms and consequently two separate indexes can be introduced: the pure cyclic fatigue damage index, referred to as D_f, and the ratcheting one D_a. The former measures the damage due to degrading or ageing, whereas the latter accounts for the damage due to a significantly dangerous event.

The maximum level that each of the two damage indexes can individually achieve (i.e. 100%) corresponds to the following: (i) the state of fatigue failure of at least one of the structural components (for D_f), and (ii) the lateral (buckling or instability) collapse of the structure triggered by the stiffness reduction due to accumulated plasticity (for D_a).

5.1. Cyclic behaviour and the D_f index

One of the basic aspects when studying cycling loads effects is predicting the fatigue life of the structure subjected to a stress–strain time history. Complete information about the behaviour of the material subjected to cyclic loading is necessary to make this prediction, in addition to the characterisation of the cyclic stress–strain response. Fatigue life is the number of loading cycles that a given structure component sustains before failure.

In the considered prototype model, fatigue failure occurs after a number of cycles of the order of 10^3 [55,56], which is a relatively small number for fatigue problems. For this reason, it is more appropriate to refer to low-cycle fatigue. Low fatigue cycle is based on the analysis of strain life because the account in terms of stress (usually considered in the prediction of high-cycle fatigue life) is less useful; furthermore, material strain offers a simpler description.

There are two strain components that characterise the cyclic stress–strain curve: the linear-elastic part ε_E and the plastic strain ε_P. For this reason, the total strain–life equation is made up of an elastic and plastic terms. The elastic strain–life term is known as Basquin's equation [57]

$$\frac{\Delta\varepsilon_E}{2} = \frac{\sigma_f^{'}}{E}(2N)^b, \tag{1}$$

where $\Delta\varepsilon_E/2$ is the elastic strain amplitude, $\sigma_f^{'}$ is a material parameter known as the fatigue strength coefficient, E is the Young's modulus, $2N$ is the number of reversals to failure (N cycles) and b is an empirical constant referred to as the strength ductility exponent. The plastic strain–life term is characterised by the Coffin–Manson relation [58,59]

$$\frac{\Delta\varepsilon_P}{2} = \varepsilon_f^{'}(2N)^c, \tag{2}$$

where $\Delta\varepsilon_P/2$ is the plastic strain amplitude, $\varepsilon_f^{'}$ is an empirical constant referred to as the fatigue ductility coefficient and c is an empirical constant known as the fatigue ductility exponent. The combined total strain is known as the strain–life equation:

DOI: 10.1002/stc

$$\frac{\Delta\varepsilon}{2} = \frac{\Delta\varepsilon_E}{2} + \frac{\Delta\varepsilon_P}{2} = \frac{\sigma_f^{'}}{E}(2N)^b + \varepsilon_f^{'}(2N)^c. \tag{3}$$

The parameters of the model (3) are reported in Table III (the Young's modulus is reported in Table I). The fatigue ductility and strength properties of the considered 6060-T6 aluminium alloy are obtained experimentally [60]. The elastic, plastic and total strain–life curves obtained with these parameters are shown in Figure 14.

The damage coefficient D_f is evaluated by the damage accumulation hypothesis; the most widely used cumulative damage form is the Palmgren–Miner's rule [61,62], which states that the failure occurs when

$$D_f = \frac{n}{N} \tag{4}$$

reaches the saturation value 1. In Eq. (4), n is the number of the applied load cycles and N is the pertinent fatigue life predicted by Eq. (3). Usually, the load cycles have not the same amplitude so that one has to consider the pertinent fatigue life for each strain amplitude. The Palmgren–Miner's rule becomes

$$D_f = \sum_{i=1}^{K} \frac{n_i}{N_i}, \tag{5}$$

where K is the number of the different strain amplitudes $\Delta\varepsilon_i$, n_i is the number of load cycles applied with one of these strain amplitudes and N_i is the associated fatigue life, again obtained by Eq. (3) with the given $\Delta\varepsilon_i$. In this case, the damage accumulation is supposed to be linear and obtained by summing up the contribution of all load cycles.

A drawback of the considered model (5) is that the fatigue life is independent of the order of application of cyclic strains of different amplitude. In spite of this, it seems to be adequate for the present purposes.

An important aspect of fatigue life prediction is the identification of the peaks (needed to compute the applied strain amplitude $\Delta\varepsilon_i$, with which we compute the N_i appearing in Eq. (5) by means of Eq. (3) and counting (necessary to detect n_i in Eq. (5). Because in this work the input is sinusoidal, the identification of the peaks is simple.

Table III. The cyclic stress–strain curve parameters for the 6060-T6 aluminium alloy.

$\sigma_f^{'}$ [MPa]	b	c	$\varepsilon_f^{'}$
376.5	−0.084	−0.537	0.157

Fatigue strength coefficient $\sigma_f^{'}$, fatigue strength exponent b, fatigue ductility exponent c and fatigue ductility coefficient $\varepsilon_f^{'}$.

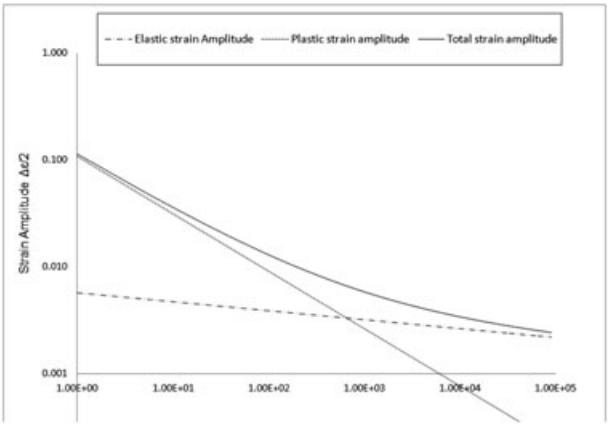

Figure 14. Total strain–life curve for 6060-T6 aluminium alloy.

DOI: 10.1002/stc

5.2. Ratcheting plastic strain and the D_a index

Cyclic plastic strain accumulation, namely, ratcheting, is a phenomenon that can occur with the application of cyclic loads characterised by constant stress amplitude with a *non-zero mean strain*. The effect P-Δ, explained in Section 4.3, could cause this phenomenon to amplify the lateral displacement. The plastic displacement causes the inter-storey drift to become so large that the original shape of the structure is altered and undergoes collapse because of the instability.

The damage component due to ratcheting has been considered in this work by taking directly into account the ratio between inter-storey drift Δ^{rel} obtained during test, the yield displacement Δ^{yield} obtained analytically and the ultimate displacement Δ^{lim} calculated from the pushover analysis (Section 4.3)

$$D_a = \frac{\Delta^{\text{rel}} - \Delta^{\text{yield}}}{\Delta^{\text{lim}} - \Delta^{\text{yield}}}. \tag{6}$$

The inter-storey drift Δ^{rel} is obtained from

$$\Delta^{\text{rel}} = \overline{\Delta} + \Delta^{\text{cyc}}, \tag{7}$$

where $\overline{\Delta}$ is the average displacement and Δ^{cyc} is the cyclic displacement. This damage index is activated when displacement reaches the value Δ^{yield} obtained analytically (Appendix A), that is, if $\Delta^{\text{rel}} \leq \Delta^{\text{yield}}$, D_a is considered equal to zero.

6. EXPERIMENTAL RESULTS

After a preliminary characterisation of material properties and a manual tuning of the numerical model, and after experimental determination of the natural frequencies, damping and modes carried out in Section 3, structural responses are now analysed in order to obtain the damage indexes. Specific cyclic failure tests have been performed. More precisely, the procedure adopted for each test is characterised by the following steps:

- Identification of modal parameters for tuning the numerical model by OMA analysis;
- Non-linear static analysis in order to obtain the preliminary capacity curve of the structures with the P-Δ effect;
- Experimental test during which a harmonic cyclic load exciting the first natural frequency in the elastic–plastic range is applied to lead the structure to collapse;
- Post-processing the measured data to determine the damage level by means of damage indexes.

We tested various identical prototypes in order to have robust results and a comprehensive understanding of the mechanical behaviour and report the results of the distinguished mechanical features.

Data are acquired at a sample rate of 1000 Hz. Time histories are acquired for 300 s. The identification of dynamic characteristics are carried on not only preliminarily for model calibration as illustrated in Section 3 but also during tests in order to detect the evolution of structural features for model updating. This has been carried out by temporarily stopping the high amplitude cyclic load and by temporarily applying a low amplitude white noise excitation needed for the OMA analysis. In the cyclic damage index estimation, the white noise inputs intervals are not considered because the input amplitude is negligible.

Three types of damages are observed in different experimental tests (Figure 15): small horizontal surface microfractures on the lateral skin of the pillars due to bending deformation (*type 1*), the local damage due to breaking of at least one of the pillars in one end due to fatigue (*type 2*) and the global collapse for bending instability due to the plastic strain accumulation (*type 3*).

Damage *type 2* and *type 3* are often independent: only in some cases, there is a rupture of the ending section of a pillar and after the collapse is reached, while sometime the bending instability (Figure 6) is reached without any local crack because of fatigue damage. It depends on the amplitude of cyclic inputs. The damage *type 1* is not considered in this study because it is simply due to overcoming of the elastic limit.

DOI: 10.1002/stc

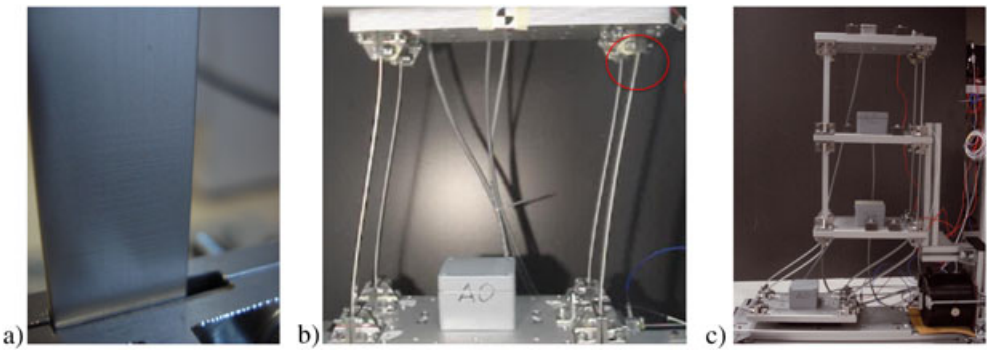

Figure 15. The three types of damage: (a) *type 1*, (b) *type 2* and (c) *type 3*.

6.1. Fatigue damage index D_f

Low-cycle fatigue life is obtained calculating cyclic strain from relative displacement. The relative displacement (inter-storey drift) are obtained from a double integration of the relative acceleration, obtained from the difference between the acceleration of the first storey and that of the base, both acquired during tests (ACC. #0 and ACC. #1, respectively). The double integration scheme used to obtain the inter-storey drift is illustrated in Figure 16, where it is shown that to have reliable results two in series high pass filters are necessary to remove low frequencies noise.

To check the effectiveness of the numerical integration, the displacement obtained from the double integration of the acceleration of the first storey (ACC. #1) is compared with that obtained by a USB imaging device that record the displacement of the same storey. The camera system allows to acquire a select One-Shot Image into LabVIEW 2010 with DirectShow imaging device support. The comparison between the signals obtained by the different procedures is reported in Figure 17 and shows a good agreement.

Displacement time histories like those of Figure 17 are used for peak counting, that is, for computing n_i in Eq. (5). They are also used to determine the relative displacement, which is then applied to the

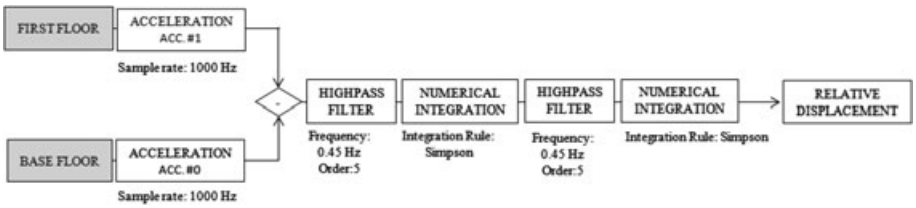

Figure 16. Scheme for double integration.

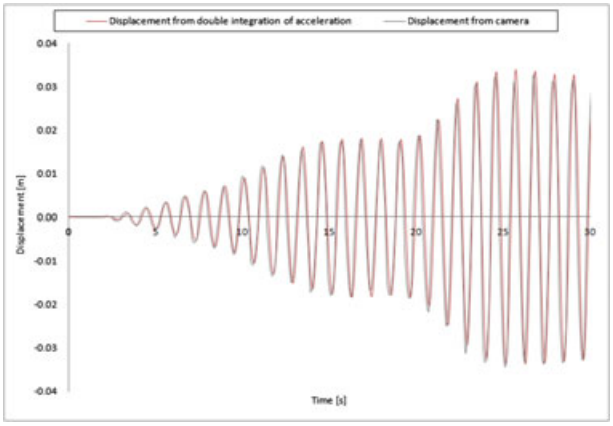

Figure 17. Comparison between numerical and experimental displacements of the first storey.

DOI: 10.1002/stc

distributed plasticity numerical model to obtain, with a non-linear static analysis, the relative strain amplitude $\Delta\varepsilon_i$ in the most stressed cross section. This latter is then is used in the Coffin–Manson's Eq. (3) to obtain the fatigue life N_i.

An example of applied load is reported in Table IV, while in Table V the associated amplitude of relative accelerations measured on the first storey, the relative number of cycles (obtained using a peak-detect function), the inter-storey drift, the strain amplitude, the maximum number of reversal with that strain amplitude and the cyclic damage index are reported. As noted in the caption, we soon have a damage of *type 1*, that is, small microcracks on the lateral side of the pillars. Later, after 4920 s and

Table IV. An example of sequence of loads.

Load step number *LS*	Type of load	Time of acquisition [s]
1	White noise	300
2	Sinusoidal input	600
3	White noise	300
4	Sinusoidal input	720
5	White noise	300
6	Sinusoidal input	720
7	White noise	300
8	Sinusoidal input	480
9	White noise	300
10	Sinusoidal input	960
11	White noise	300
12	Sinusoidal input	1440
13	White noise	300
14	Sinusoidal input	240

Table V. Measured and post-processed quantities needed for the local damage analysis.

LS	t_i [s]	a_1^{rel} [ms^{-2}]	n_i	Δ_i^{cyc} [m]	$\Delta\varepsilon/2$	N_i	D_f [%]	TD
2	120	1.06	88	0.031	0.0027	21 142	0.4	None
2	360	1.18	200	0.033	0.0029	12 696	2.0	None
2	496	1.31	111	0.036	0.0033	7419	3.5	Type 1
2	600	1.42	89	0.038	0.0035	5033	5.3	Type 1
4	840	1.23	162	0.035	0.0033	7415	7.4	Type 1
4	1080	1.38	210	0.037	0.0035	5345	11.4	Type 1
4	1320	1.41	207	0.038	0.0035	5025	15.5	Type 1
6	1560	1.47	190	0.038	0.0036	4626	19.6	Type 1
6	1680	1.39	57	0.038	0.0035	4903	20.8	Type 1
6	1800	1.29	136	0.035	0.0033	6541	22.8	Type 1
6	2040	1.43	193	0.038	0.0036	4636	27.0	Type 1
8	2280	1.34	175	0.037	0.0034	5558	30.2	Type 1
8	2520	1.61	183	0.040	0.0038	3503	35.4	Type 1
10	2760	1.66	176	0.039	0.0037	3790	40.0	Type 1
10	3000	1.71	156	0.039	0.0037	3787	44.1	Type 1
10	3240	1.27	165	0.044	0.0044	1881	52.9	Type 1
10	3480	1.23	144	0.038	0.0039	3175	57.4	Type 1
12	3720	1.6	201	0.039	0.0040	2872	64.4	Type 1
12	3785	1.29	38	0.035	0.0035	4859	65.2	Type 1
12	3960	1.56	139	0.039	0.0039	3028	69.8	Type 1
12	4100	1.36	108	0.038	0.0038	3414	73.0	Type 1
12	4200	1.67	69	0.040	0.0040	2803	75.4	Type 1
12	4440	1.59	159	0.040	0.0040	2854	81.0	Type 1
12	4480	1.03	24	0.031	0.0032	7714	81.3	Type 1
12	4680	1.41	117	0.042	0.0042	2235	86.6	Type 1
12	4920	1.63	126	0.042	0.0042	2236	92.2	Type 1
14	5160	1.18	151	0.034	0.0035	5351	95.0	Type 2

Load step number *LS* (see Tab. IV), elapsed time t_i, relative acceleration amplitude measured at each step a_1^{rel}, total number of cycles at each step n_i, relative cyclic displacement amplitude at each step Δ_i^{cyc}, cyclic strain amplitude at each step $\Delta\varepsilon/2$, maximum number of reversal at each level of strain N_i, cumulative cyclic damage index D_f, type of damage TD.

DOI: 10.1002/stc

3600 cycles, one pillar undergoes a macrocrack and then breaks, that is, a local damage of *type 2* occurs. It is worth to underline that the macrocrack occurs when D_f is close to 100%, a fact that proves the reliability of D_f, at least in this case. In Figure 18, we show the evolution of the first resonant frequency with damage progression, obtained by OMA processing the output signals measured during the load steps in which the input exciting the system is a white noise sequence. Its reduction is a further confirmation of the progress of the damage, which reduces the stiffness and thus the natural frequencies.

6.2. Ratcheting damage index D_a

The global damage index is considered in this work by taking into account the ratcheting damage index D_a expressed by Eq. (6). The total relative displacement Δ^{rel} is the maximum inter-storey drift between the ground and the first storey, because the pillars between these two storeys are the most stressed. The cyclic displacement Δ^{cyc} is obtained from the double integration of the relative acceleration.

The mean displacement $\overline{\Delta}$ increases linearly in time (an example is reported in Figure 19), so that it cannot be obtained by the double integration of the accelerations, because the initial velocity is not

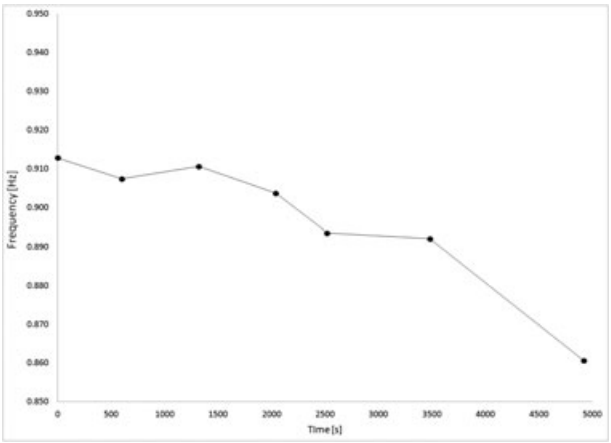

Figure 18. Evolution of the first resonant frequency with damage progression, obtained for the sequence of loads reported in Table IV.

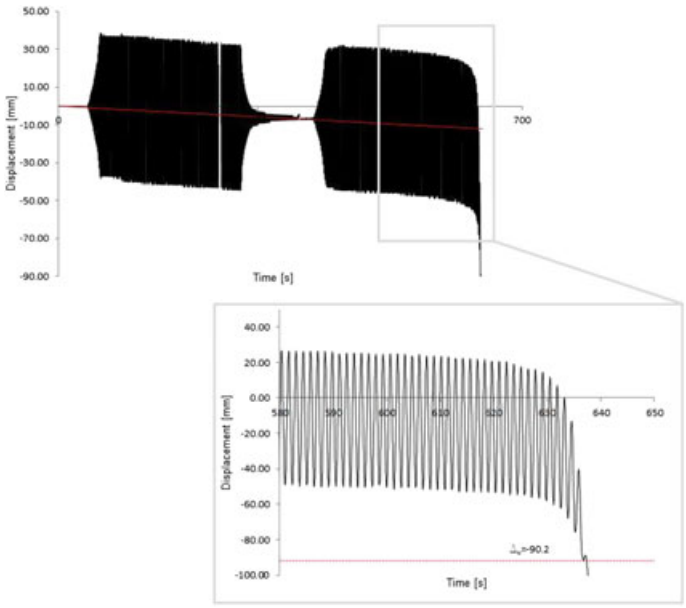

Figure 19. Displacement amplitude of the first storey during different progressive tests and last steps before collapse.

DOI: 10.1002/stc

known. Thus, it must be computed in a different manner, by a non-linear dynamic analysis of the FEM numerical model. A non-linear dynamic analysis of the model is performed, in order to simulate ratcheting behaviour, and the reliability of the numerical model results is checked by comparing these values with the experimental time histories acquired with the camera. Because we have verified that the displacements obtained with the camera are in good agreement with those obtained with the numerical model, in the present work, we use the former only because they are easier to handle. Of course, in real applications, the displacements to be used will be those coming from the numerical model. An example of the camera-recorded time histories is shown in Figure 19.

The sequence of loads applied to another (i.e. not the same considered in Section 6.1 but with the same materials and geometry) prototype model is reported in Table VI, while in Table VII the relevant quantities of interest are given. The results demonstrate that the ultimate displacement predicted with static non-linear analysis ($\Delta_{\lim} = 0.092$ m, Section 4.3) is consistent with the real displacement measured just before collapse. In fact, one can observe that the structure collapses because of structural instability (*type 3*) when it achieves the maximum level of damage index $D_a \simeq 100\%$. Note that in the meantime D_f remains well below the critical threshold.

6.3. Numerical simulations

As previously said, in the considered low-cost monitoring system, the displacement can be obtained by a non-linear dynamic analysis of the FEM numerical model in order to compute the cycles' amplitude and the ultimate displacement before collapse.

In order to numerically simulate the previous experimental test, and to check the effectiveness of the double numerical integration of the experimental accelerations, the harmonic acceleration recorded during the test is applied at the base nodes of the numerical model. In this case, a distributed plasticity model as described in Section 4.2 is considered.

The differential equations of motion are integrated numerically by the *Newmark* method. The accuracy of this method depends on the integration step, which is chosen on the basis of the period of the excitation, of the natural period T_n of the structure and of the input sampling frequency. A good balance between accuracy and rapidity of the integration is obtained with the integration step $\Delta t = 0.0005$ s.

Table VI. A typical sequence of loads.

Load step number *LS*	Type of load	Time of acquisition [*s*]
1	White noise	300
2	Sinusoidal input	180
3	White noise	300
4	Sinusoidal input	158

Table VII. Measured and post-processed quantities needed for the global damage analysis.

LS	t_i [s]	Δ^{rel} [m]	D_a [%]	TD
2	60	0.0406	17.06	None
2	120	0.0402	16.52	None
2	180	0.0403	16.67	None
4	300	0.0456	25.21	None
4	320	0.0457	25.34	None
4	322	0.0489	30.48	None
4	324	0.0515	34.68	Type 1
4	326	0.0547	39.84	Type 1
4	328	0.0564	42.58	Type 1
4	330	0.0576	44.52	Type 1
4	332	0.0594	47.42	Type 1
4	334	0.0666	59.03	Type 1
4	336	0.0739	70.81	Type 1
4	338	0.0902	97.1	Type 3

Load step number *LS* (see Tab. VI), elapsed time t_i, total relative displacement Δ^{rel}, ratcheting damage index D_a, type of damage TD.

DOI: 10.1002/stc

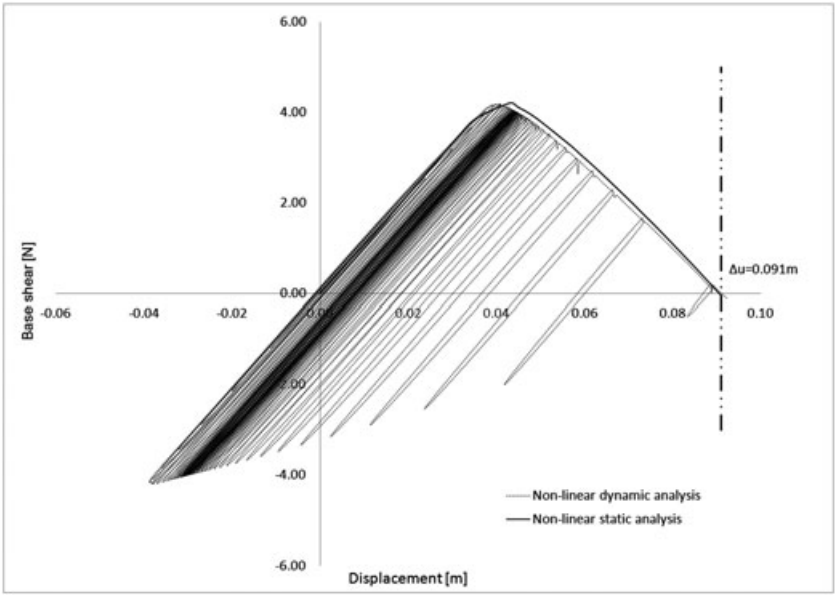

Figure 20. Base shear versus displacement of the first storey, from static and dynamic non-linear analysis.

The results of the numerical integrations are illustrated in Figure 20, where we report the lateral displacement versus the base shear force. We choose this type of representation, instead of a classical time history, because it permits to visualise the decrement of the lateral strength of the frame with increasing number of cycles and, moreover, because it allows to perform a comparison with the results of the static non-linear (push-over) analysis obtained in Section 4.3.

We note that there is a good agreement between the non-linear dynamic and non-linear static analyses. As a matter of fact, this shows that the ultimate displacement Δ_u predicted with the preliminary non-linear static analysis, and used for the ratcheting damage index D_a, is consistent with numerical and experimental results.

Starting from the first cycles, the lateral displacement of the first storey overcomes the yield lateral displacement, which is equal to $\Delta^{\text{yield}} = 0.03$ m (Appendix A). Thus, there is a plasticity accumulation, and the structure undergoes at each cycle a permanent shift in one direction, while the lateral resistance of the structure decreases to zero.

The ultimate displacement Δ_u predicted by the numerical model, which is shown in Figure 20 and which is the amplitude of the last cycle before the numerical analysis divergence in correspondence of a zero lateral resistance, is equal to that obtained from experimental test (Figure 19), in correspondence of which the structure collapses because of the lateral instability.

7. CONCLUSIONS

In this work, a novel combined experimental and numerical methodology to perform the SHM of civil structures lying in seismic hazard zones is proposed.

A prototype frame model of a three-storey building has been build up and instrumented in order to simulate the vibration response of a multistorey building subjected to seismic loads. In this stage, we neglected all the effects that are typical of a real structure in a real environment. Specifically, we did not consider the effects related to noise in the measurements, specific structural typologies and boundary conditions, complexity (where to put sensors and how many), low and high amplitude cyclic behaviour of reinforced concrete and masonry, the occurrence of soil–structure interaction, and others, according to the fact that only the proof of the concept has been sought in this work. These aspects will be investigated in future developments.

Two different FEM models (with lumped and distributed plasticity) of the prototype have been developed and manually tuned up, making usage of parameters identified by an OMA of the structure.

DOI: 10.1002/stc

After having verified the reliability of monitoring system and numerical models, the real structure behaviour has been studied not only in the elastic range but also in the plastic one. In this way, the cyclic stress–strain relationship and displacement time histories due to strong motion have been investigated and compared with experimental results. This kind of analysis has been used to extrapolate local and global indexes of damage, used to forecast the remaining structure lifetime.

By the experimental investigation performed in this research, several fundamental aspects have been treated: (i) the preliminary experimental results of the proposed combined methodology, obtained, in laboratory, by testing the three-storey aluminium scaled frame; (ii) the study of the monotonic behaviour, up to failure, to understand the mechanism that could cause collapse (the P-Δ effect); (iii) the cyclic fatigue behaviour, for a fixed value of the imposed displacement, to understand the mechanism that produces the cyclic damage; and (iv) the cyclic behaviour in terms of plastic accumulation, to determine how the damage due to cyclic load leads to collapse.

The structural damage has been related to two different mechanisms, and consequently, two separate indexes have been introduced: the pure cyclic fatigue damage index, referred to as D_f, and the ratcheting one, D_a.

The damage estimation methodology is verified by comparing the experimental results with the model prediction during cyclic failure tests.

The life prediction for the prototype model, obtained by damage indexes, estimated from the measurements acquired by a low-cost SHM system, has proved to be consistent with the experimental results.

The results obtained up to now have shown that the numerical model damage calculation and the failure prediction are reliable, at least in the considered case. As said, the scope of this work was to check the feasibility of the proposed SHM technique. This has been performed by using the experimental model, which has natural frequencies similar to those of real structures, but very different damage behaviour. However, we do not believe that this is a drawback. In fact, once the damage laws for RC or masonry buildings were identified, they could be easily implemented in the model, and, after a proper trial-and-error preliminary tuning, the procedure could be applied to real structures.

APPENDIX A. ANALYTICAL RESULTS CONSIDERING P-Δ EFFECT

The linear Euler–Bernoulli beam theory extended with P-Δ effect is considered in order to take into account the influence of axial force on the bending stiffness on the first storey because only this floor is clearly influenced by this effect (see Section 4.3 for references). For this reason, a clamped–clamped beam with constant axial force, P, which is positive in compression, is taken into account. The differential governing equation is

$$\frac{d^4x}{dz^4} + \alpha^2 \frac{d^2x}{dz^2} = 0, \tag{A1}$$

where $\alpha^2 = P/EJ$. The general solution of the previous equation is

$$x(z) = C_1 \cos\, \alpha z + C_2 \sin\, \alpha z + C_3 z + C_4. \tag{A2}$$

By considering that the pillars of the first storey have no constant cross section (Figure A1 and Table AI) and by taking into account the boundary (clamped in A, given Δ displacement in B) and the continuity conditions (in C and D), one finds that

$$\Delta^{\text{yield}} = \frac{\chi^{\text{yield}}}{0.7887\alpha^2 \cos(\alpha L) + 0.628\alpha^2 \sin(\alpha L)}, \tag{A3}$$

where χ^{yield} is the yield curvature attained at the beam ends (point B) and Δ^{yield} is the corresponding displacement.

In the considered case, we acquire $\Delta^{\text{yield}} = 0.03$ m, while the yield moment M_Δ^{yield} and shear V_Δ^{yield} for each pillar are reported in Table AII.

In conclusion, the stiffness of each pillar belonging to the first storey is $k_\Delta = V_\Delta^{\text{yield}} \left(\Delta^{\text{yield}}\right)^{-1} = 120.04$ N/m.

DOI: 10.1002/stc

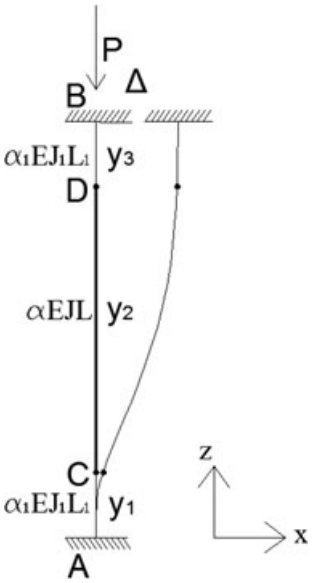

Figure A1. Sketch of the considered structure.

These results are used to calibrate the moment–rotation relationship for the plastic hinge of the lumped model. In fact, the moment on yield limit $M'^{\text{yield}}_{\Delta}$ for the lumped plasticity model is obtained from

$$M'^{\text{yield}}_{\Delta} = \frac{M^{\text{yield}}_{\Delta}}{k}. \tag{A4}$$

$M'^{\text{yield}}_{\Delta}$ is an amplified value of $M^{\text{yield}}_{\Delta}$ (k is equal to 0.7), and it is considered in order to match the plastic range behaviour and to obtain the same ultimate displacement Δ_u of the distributed plasticity model (shown in Figure 12). In fact, matching the exact yield value of displacement Δ^{yield} of the distributed model, the ultimate displacement Δ_u is underestimated. In Table AIII, the values of the moment–rotation relationship of each non-linear link are reported. These values are calibrated by the comparison between the same static-scheme modelled with a distributed plasticity model.

Table AI. Geometrical and mechanical characteristic values.

P [N]	α_1[m^{-1}]	α[m^{-1}]	J_1[m^4]	J[m^4]	L[m]	L_1[m]	h[m]	h_1[m]
33.25	11.15	7.098	4.05E-12	1E-11	0.196	0.028	0.002	0.00148

Table AII. Displacement, moment and shear on yield limit.

Δ^{yield}[m]	$M^{\text{yield}}_{\Delta}$[Nm]	$V^{\text{yield}}_{\Delta}$[N]
0.03	0.9583	3.62

Table AIII. Moment–rotation relationship of non-linear link.

	Rotation θ [rad]	$M'^{\text{yield}}_{\Delta}$ [Nm]
Yield limit	0	1.369
Collapse limit	0.040	1.415

DOI: 10.1002/stc

ACKNOWLEDGEMENTS

This work has been partially supported by the Italian Ministry of Education, University and Research (MIUR) by the PRIN funded programme 2010/11 N.2010MBJK5B 'Dynamics, stability and control of flexible structures'.

REFERENCES

1. Ibarra LF, Krawinkler H. *Global collapse of frame structures under seismic excitations*. Report No. PEER 2005/06, Pacific Earthquake Engineering Research Center, University of California: Berkeley, CA, 2005.
2. European Committee for Standardization (CEN). 2013. *Eurocode 8: design of structures for earthquake resistance – part 1*: *general rules*, seismic actions and rules for buildings. EN 1998–1:2004/A1:2013
3. Shih HW, Thambiratnam DP, Chan THT. Damage detection in slab-on-girder bridges using vibration characteristics. *Structural Control & Health Monitoring* 2013; **20**(10):1271–1290. doi:10.1002/stc.1535.
4. Ji X, Fenves G, Kajiwara K, Nakashima M. Seismic damage detection of a full-scale shaking table test structure. *Journal of Structural Engineering* 2011; **137**(1):14–21.
5. Cunha A, Caetano E, Magalhães K, Moutinho C. Recent perspective in dynamic testing and monitoring of bridges. *Structural Control & Health Monitoring* 2013; **20**(6):853–877. doi:10.1002/stc.1516.
6. Cosenza E, Manfredi G. Damage index and damage measures. *Progress in Structural Engineering and Materials* 2000; **2**:50–59.
7. Xiaodong J, Jiaru Q, Longhe X. Damage diagnosis of a two-storey spatial steel braced-frame model. *Structural Control & Health Monitoring* 2007; **14**(8):1083–1100.
8. Rytter T. *Vibration Based Inspection of Civil Engineering Structure*. PhD dissertation, Department of Building Technology and Structure Engineering, Aalborg University: Denmark, 1993.
9. Worden K, Farrar CR, Haywood J, Todd M. A review of nonlinear dynamics applications to structural health monitoring. *Structural Control & Health Monitoring* 2008; **15**(4):540567.
10. Yan YJ, Cheng L, Wu ZY, Yam LH. Development in vibration-based structural damage detection technique. *Mechanical System and Signal Processing* 2007; **21**:2198–2211.
11. Deraemaeker A, Reynders E, Roeck GD, Kullaa J. Vibration-based structural health monitoring using output-only measurements under changing environment. *Mechanical Systems and Signal Processing* 2008; **22**(1):34–56.
12. Gentile C, Gallino N. Condition assessment and dynamic system identification of a historic suspension footbridge. *Structural Control & Health Monitoring* 2008; **15**:369–388.
13. Farrar CR, Doebling SW, Nix DA. Vibration-based structural damage identification. *Philosophical Transactions of the Royal Society of London A* 2001; **359**:131–149.
14. Doebling S. *Measurement of Structural Flexibility Matrices for Experiments With Incomplete Reciprocity*. PhD dissertation, Department of Aerospace Engineering, University of Colorado: Boulder, CO, 1995.
15. Alvandi A, Cremona C. Assessment of vibration-based damage identification techniques. *Journal of Sound and Vibration* 2006; **292**:179–202.
16. Aras F, Krstevska L, Altay G, Tashkov L. Experimental and numerical modal analyses of a historical masonry palace. *Construction and Building Materials* 2011; **25**(1):81–91.
17. Bernal D, Gunes B. A flexibility based approach for the localization and quantification of damage: a benchmark application. *Journal of Engineering Mechanics* 2004; **130**:61–70.
18. Brandt A. *Noise and Vibration Analysis*: *Signal Analysis and Experimental Procedures*. John Wiley & Sons, Chichester, West Sussex, United Kingdom, 2010; ISBN: 978-0-470-74644-8.
19. Brownjohn JMW, De Stefano A, Xu YL, Wenzel H, Aktan AE. Vibration-based monitoring of civil infrastructures: challenges and successes. *Journal of Civil Structural Health Monitoring* 2011; **1**(3–4):79–95.
20. Cabboi A, Gentile C, Saisi A. *Vibration-based SHM of a Centenary Bridge*: *a Comparative Study Between two Different Automated OMA Techniques*. Proc. of EURODYN2014: Porto, Portugal, 2014.
21. JE Mottershead JE, Friswell MI. Model updating in structural dynamics: a survey. *Journal of Sound and Vibration* 1993; **167**(2):347–375.
22. Ragland WS, Penumadu D, Williams RT. Finite element modeling of a full-scale five-girder bridge for structural health monitoring. *Structural Health Monitoring* 2011; **10**(5):449–465.
23. Gičev V, Trifunac MD. A note on predetermined earthquake damage scenarios for structural health monitoring. *Structural Control & Health Monitoring* 2012; **19**(8):746–757.
24. Colombo A, Negro P. A damage index of generalized applicability. *Engineering Structures* 2005; **27**:1164–1174.
25. Tibaduiza DA, Mujica LE, Rodellar J. Damage classification in structural health monitoring using principal component analysis and self-organizing maps. *Structural Control & Health Monitoring* 2013. **20**(10):1303–1316. doi:10.1002/stc.1540.
26. Miranda E, Asce M, Akkar SD. Dynamic instability of simple structural systems. *Journal of Structural Engineering* 2003; **129**:1722–1726.
27. Asimakopoulos AV, Karabalis DL, Beskos DE. Inclusion of p-δ effect in displacement-based seismic design of steel moment resisting frames. *Earthquake Engineering & Structural Dynamics* 2007; **36**:2171–2188.
28. Morita K, Teshigawara M, Hamamoto T. Detection and estimation of damage to steel frames through shaking table tests. *Structural Control & Health Monitoring* 2005; **12**(3–4):357–380.
29. Duy Y, Zhenlin W. A new approach to low-cycle fatigue damage based on exhaustion of static toughness and dissipation of cyclic plastic strain energy during fatigue. *International Journal of Fatigue* 2001; **23**(8):679–687.
30. *MMA 7361L Technical Data*, Tech. rep., Freescale Semiconductor Inc., Document Number MMA 7361L Rev0 2008.
31. *LIS2L02AS4 Datasheet*, T. rep., ST Microelectronics Group, rev 2 2005.
32. Albarbar A, Mekid S, Starr A, Pietruszkiewicz R. Suitability of MEMS accelerometers for condition monitoring: an experimental study. *Sensors* 2008; **8**:784–799.
33. Ruzziconi L, Younis MI, Lenci S. An electrically actuated imperfect microbeam: dynamical integrity for interpreting and predicting the device response. *Meccanica* 2013; **48**:1761–1775.

34. Mohd-Yasin F, Korman CE, Nagel DJ. Measurement of noise characteristics of MEMS accelerometers. *Solid-State Electronics* 2003; **47**:357–360.
35. Albarbar A, Badri A, Jyoti K, Sinha AS. Performance evaluation of MEMS accelerometers. *Measurement* 2009; **42**(5): 790–795.
36. Khine A, Mon M, Tin B, Nwe T, Dr C, Naing ZM, Dr D, Myint YM. Analysis on modeling and simulation of low cost MEMS accelerometer ADXL202. *Proceedings of World Academy of Science: Engineering & Technology*, 2008; **44**, p.598.
37. Brincker R, Henning Kirkegaard P. Special issue on operational modal analysis. *Mechanical Systems and Signal Processing* 2010; **24**:1209–1323.
38. Hermans L, Van der Auweraer H. Modal testing and analysis of structures under operational conditions: industrial applications. *Mechanical Systems and Signal Processing* 1999; **13**:193–216.
39. Antonacci E, De Stefano A, Gattulli V, Lepidi M, Matta E. Comparative study of vibration-based parametric identification techniques for a three-dimensional frame structure. *Structural Control & Health Monitoring* 2012; **19**:579–608.
40. Peeters B, Van der Auweraer H, Vanhollebeke F, Guillaume P. Operational modal analysis for estimating the dynamic properties of a stadium structure during a football game. *Shock and Vibration* 2007; **14**:283–303.
41. Soria L, Peeters B, Anthonis J, Van der Auweraer H. Operational modal analysis and the performance assessment of vehicle suspension systems. *Shock and Vibration* 2012; **19**:1099–1113.
42. Heylen W, Lammens S, Sas P. *Modal Analysis Theory and Testing*. K.U.Leuven: Leuven, Belgium, 2007.
43. Peeters B, Van der Auweraer H, Guillaume P, Leuridan J. The PolyMAX frequency-domain method: a new standard for modal parameter estimation? *Shock and Vibration* 2004; **11**:395–409.
44. Van der Auweraer H, Guillaume P, Verboven P, Vanlanduit S. Application of a fast-stabilizing frequency domain parameter estimation method. *ASME Journal of Dynamic Systems, Measurement, and Control* 2001; **123**:651–658.
45. Van Overschee P, De Moor B. 1996. *Subspace Identification for Linear Systems Theory – Implementation – Applications*, K.U.Leuven, Leuven, Belgium, KLUWER ACADEMIC PUBLISHERS Boston/London/Dordrecht.
46. European Committee for Standardization (CEN). 2007. *Eurocode 9*: *Design of aluminum structures*. *Part.1-1*: *structural rules*. EN 1999-1-1:2007.
47. Chaboche JL. 2013. *Cumulative Damage*, *in Fatigue of Materials and Structures*: *Application to Design and Damage* Bathias C, Pineau A (eds). John Wiley & Sons, Inc.: Hoboken, NJ, USA. doi: 10.1002/9781118616994.ch2
48. Mancini E, Isidori D, Sasso M. 2012. *Caratterizzazione del comportamento plastico-ciclico di strutture flessibili mediante applicazione del modello di Chaboche*. Proceeding of 41st National Congress AIAS 2012, Associazione Italiana per L'Analisi delle Sollecitazioni, University of Padua, Vicenza (in Italian).
49. Coleman J, Spacone E. Localization issues in force-based frame elements. *Journal of Structural Engineering* 2001; **127**(11): 1257–1265.
50. Benavent-Climent A, Zahran R. An energy-based procedure for the assessment of seismic capacity of existing frames: application to RC wide beam systems in Spain. *Soil Dynamics and Earthquake Engineering* 2010; **30**(5):354–367.
51. Adam C, Jager C. Seismic collapse capacity of basic inelastic structures vulnerable to the P-delta effect. *Earthquake Engineering and Structural Dynamics* 2012; **41**(4):775–793. doi:10.1002/eqe.1157.
52. Kobayashi M, Ohno N. Implementation of cyclic plasticity models based on a general form of kinematic hardening. *Int. J. Numer. Meth. Engng.* 2002; **53**(9):2217–2238. doi:10.1002/nme.384.
53. Bernal D. Instability of buildings during seismic response. *Engineering Structures* 1998; **20**(4–6):496–502.
54. Ahmadzadeh GR, Varvani-Farahani A. Triphasic ratcheting strain prediction of materials over stress cycles. *Fatigue & Fracture of Engineering Materials & Structures* 2012; **35**(10):929–935.
55. Boardman D. Fatigue resistance of steels. *ASM handbook, properties and selection: irons, steels, and high-performance alloys*. *ASM International* 1990; **1**:673–688.
56. Yao J, Munse W. *Low-cycle Fatigue of Metals*. *Literature Review*. Tech. rep., Ship Structure Committee: Washington DC, 1961.
57. Lieurade HP, Degallaix S, Degallaix G, Gauthier JP. In *Fatigue Tests*, *in Structural Components*: *Mechanical Tests and Behavioral Laws*, Franois D (ed). ISTE: London, UK, 2010. doi:10.1002/9780470611036.ch6.
58. Dowling N. *Mechanical Behavior of Materials*. Pearson Education, Upper Saddle River, NJ, 2012. ISBN-13: 9780131395060.
59. Bannantine J, Comer JJ, Handrock JL. *Fundamentals of Metal Fatigue Analysis*. Prentice Hall Englewood Cliffs, NJ, 1990. ISBN-13: 978-0133401912.
60. Borrego LP, Abreu LM, Costa JM, Ferreira JM. Analysis of low cycle fatigue in AlMgSi aluminium alloys. *Engineering Failure Analysis* 2004; **11**:715–725.
61. Miner MA. Cumulative damage in fatigue. *Journal of Applied Mechanics* 1945; **12**:A159–A164.
62. Lalanne C. *Accumulation of Fatigue Damage*, *in Fatigue Damage* (2nd edn.) Mechanical Vibration and Shock Analysis **4**. ISTE: London, UK, 2010.

DOI: 10.1002/stc